

Enhancing Surface Neural Implicits with Curvature-Guided Sampling and Uncertainty-Augmented Representations

Lu Sang Abhishek Saroha Maolin Gao Daniel Cremers
Computer Vision Group
Technical University of Munich

lu.sang, abhishek.saroha, maolin.gao, cremers@tum.de

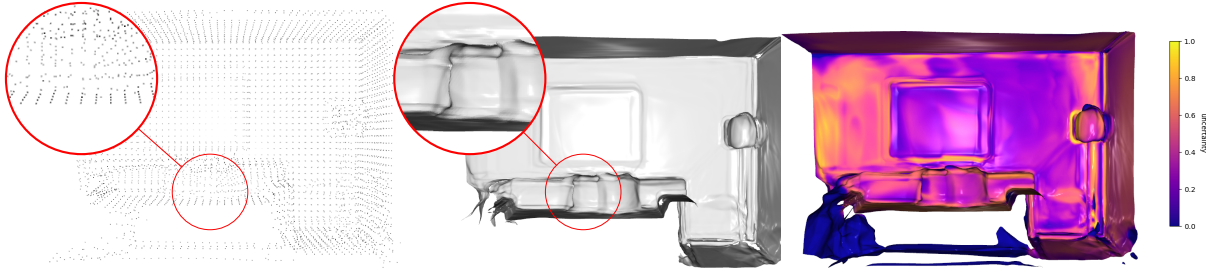


Figure 1. Reconstructed the surface (middle) of the proposed method with only a sparse input (left, $\sim 6k$ points) together with the uncertainty of each surface point (right).

Abstract

Neural implicits have become popular for representing surfaces because they offer an adaptive resolution and support arbitrary topologies. While previous works rely on ground truth point clouds, they often ignore the effect of input quality and sampling methods during reconstructing process. In this paper, we introduce a sampling method with an uncertainty-augmented surface implicit representation that employs a sampling technique that considers the geometric characteristics of inputs. To this end, we introduce a strategy that efficiently computes differentiable geometric features, namely, mean curvatures, to augment the sampling phase during the training period. The uncertainty augmentation offers insights into the occupancy and reliability of the output signed distance value, thereby expanding representation capabilities into open surfaces. Finally, we demonstrate that our method leads to state-of-the-art reconstructions on both synthetic and real-world data.

1. Introduction

It is important to reconstruct surfaces for downstream tasks. Finding a suitable surface representation is also crucial. Many methods have been proposed to train a neural network to reconstruct the surface using point cloud or mesh data. Moreover, most of the methods consider only dense and

clean input. How to deal with sparse and noise input is undiscussed. Some methods require (oriented) surface normals to produce satisfactory results. However, in real-world scenarios, the requirement on (high quality) point cloud and its (oriented) normals is often hard to fulfill, which leads to failure cases of recent reconstruction methods [8, 18]. Moreover, training data might be unevenly distributed. The selection of sampling strategies impacts both the efficacy of training and the quality of the outcomes. A natural question arises: can we adjust the sampling method according to the features of the input data and enhance the training? To address these questions, in this paper, we propose a technique that utilizes depth images as basic input and predicts the signed distance value of query points. Depth images enable us to easily estimate point normals and other surface geometry features such as curvatures. We propose a curvature-guided sampling strategy, which enhances the training process and reduces the uneven sampling problem. Moreover, this method effectively interpolates among inputs to counter the low-quality data issues. We also incorporate an uncertainty value in neural implicit representation to ascertain the reliability of the prediction. This augments the capabilities of the signed distance field to depict open surfaces without additional effort, as shown in Fig. 1. In summary, our contributions are the following.

- We introduce a novel method, which can deal with sparse input data to reconstruct surfaces ranging from single ob-

jects to large scenes using the same framework.

- We propose a method that computes mean curvature directly from input depth images and uses it as a curvature-guided sampling strategy, which considers the geometric feature of the input to enhance the training efficiency.
- We introduce an uncertainty-aware implicit neural representation that gives an uncertainty of predictions and enables open surface presentation.
- Extensive experimental studies show that our proposed method achieves state-of-the-art reconstruction results on challenging synthetic and real-world datasets.

2. Related Work

2.1. Surface Representations and Reconstructions

Surface representation Surface representation can be classified into two categories based on the stored surface properties: explicit surface representation (e.g., polygon mesh or point clouds) and implicit surface representation (e.g., signed distance field). Explicit methods struggle with complex topologies, resolution adjustments, local modifications, and potential high memory consumption when storing high-resolution surfaces. In contrast, implicit representations represent the surfaces by storing indirect information about the surface, which overcomes the shortages of explicit methods. However, **classical** implicit methods still suffer from fixed resolution and high memory consumption issues. For example, the memory consumption is $\mathcal{O}(n^3)$ for a n resolution voxel grid. Luckily, **neural** implicit representations can encode the surface implicit information such as occupancies [7, 17, 31], signed/unsigned distance functions [6, 8, 18, 32, 35, 36] into neural networks. One can query any 3D points in space to obtain the corresponding attributes. This approach allows for recovering highly detailed surfaces at a lower memory cost than traditional surface representation methods such as classical signed distance field (SDF). Moreover, it is a continuous representation suitable for further mathematical analysis of the represented surface. (Signed/unsigned) Distance Field stores the shortest (signed) distance of a given point to a surface. The gradients of an SDF provide a normal vector of the surface, but using SDF requires well-defined "inside" and "outside" notions, which restrict representing open surfaces. An unsigned distance field (UDF) does not distinguish the inside or outside. However, the lack of a sign introduces ambiguity in surface reconstruction, such as the correct surface orientation.

Surface Reconstructions Much like with surface representations, surface reconstructions techniques can be categorized into traditional approaches, including **classical** methods like Poisson surface reconstructions [24] and SSD [4]. These techniques commonly utilize point clouds as input to create a polygon mesh. Unfortunately, these traditional methods are considerably reliant on the quality of input data,

often failing when faced with complex geometries. Moreover, using traditional methods is hard to modify output resolution without repeating the complete reconstruction process. On the other hand, **learning-based** implicit surface reconstruction approaches train neural networks to generate surface features [7, 18, 32, 36, 39, 45], allowing for changing the output resolution without retraining the network. Additionally, they can handle relatively complicated geometry. The typical input of these methods is 3D data, e.g., a point cloud or a mesh [23, 36]. Some methods also need a point cloud with normals information to ensure a satisfactory result [18, 45]. Some need ground truth mesh to do supervision [35, 39]. Some gradually involve an initialized mesh to do the reconstruction, instead of learning the implicit representation [21, 39]. However, obtaining point clouds with normals is not straightforward if the ground-truth mesh is not given or the point cloud quality is poor, which often happens in real-world applications.

2.2. Training Data Sampling

Sparse training data Learning-based methods sample data from the given input to train the network to predict underlying surface features. Sampling the training data is easy when the input format, such as a mesh [35], allows for infinite sampling. When only a limited sample is available, such as in point clouds [18, 45], random sampling from the point cloud is the most common way. It leads to one problem: inefficient training data leads to bad reconstruction results [7, 8].

Biased Sampling Another problem of the random sampling is that points in the point cloud, especially the points acquired from real-world data, are not uniformly located on the surface, as discussed by [49] and [35]. Points extracted from the iso-surface will likely be gathered near high-curvature areas [49]. Plus, complex surface areas need more points to represent their features. Random sampling does not consider these effects. To avoid this issue, [49] samples on and near the iso-surface with some tolerance. [35] proposes to sample according to principal curvatures of the surface points such that the sampled points are evenly distributed according to the curvatures. They divide points into low, medium, and high curvature categories according to the absolute sum of two principal curvature κ_1 and κ_2 . However, ground-truth meshes are required in their computation pipeline.

To tackle the challenges mentioned above, in this paper, we focus on more practical inputs: depth images, which can be directly acquired from hardware. We initiate a coarse voxel grid that retains initial SDF values, normals, and curvatures derived from depth images, effectively addressing the issues related to input points with (oriented) normals. The voxel grid structure allows us to locate any query points in space to get the related attributes by efficiently interpolating

within voxels, thereby resolving the sparse input problem. Our approach leverages a hybrid representation combining point clouds and voxels, improving implicit surface reconstruction accuracy. Moreover, we embed an uncertainty value into implicit surface representation to indicate the reliability of the SDF value. The uncertainty value helps to eliminate redundant areas and facilitates the reconstruction of open surfaces. The paper is structured as follows: we introduce our method in Sec. 3, the experiments and evaluation results are stated in Sec. 4, we summarize our method in Sec. 5, more results and analysis are in the supplementary material.

3. Method

Our goal is to train a network $f(\mathbf{x}, \theta) : \mathbb{R}^3 \rightarrow \mathbb{R} \times [0, 1]$, which predicts the SDF value and uncertainty of this value, such that the wanted surface \mathcal{S} lies on the level-set $\{\mathbf{x} | f(\mathbf{x}) = 0\}$. We assume the shape \mathcal{S} is captured by a set of depth images $\{D_k\}$. We first utilize a coarse voxel grid from depth images. During the process, points normals and curvatures are computed and merged to the coarse voxels. Then we introduce a curvature-guided sampling method together with a novel interpolating method to create and select training data for each epoch. Last, we talk about extracting surface considering uncertainty. We also show that our method can easily be transplanted to other methods to improve the results.

3.1. Voxel Utilization

We utilize a coarse voxel grid $\{\mathbf{v}_i\} \subset \mathbb{R}^3$ for $i \in \mathcal{V}$ containing SDF value for each voxel following the method described in [46]. For each voxel $\mathbf{v}_i \in \mathbb{R}^3$, we initialize two local properties: the SDF value $\psi_i^v \in \mathbb{R}$ of that voxel and the uncertainty of the SDF value $w_i^v \in [0, 1]$. Larger w_i^v means the SDF value is reliable, and $w_i^v = 0$ indicates the voxel properties are not updated. Different from the traditional voxel grid, a gradient of distance $\mathbf{g}_i^v \in \mathbb{R}^3$ is also integrated for each voxel after computing the normal vector of each pixel in the depth images using FALS method [1]. The point cloud contained in the voxel can be extracted by

$$\mathbf{x}_i = \mathbf{v}_i - \hat{\mathbf{g}}_i^v \psi_i^v \quad (1)$$

where $\hat{\mathbf{g}}_i^v = \frac{\mathbf{g}_i^v}{\|\mathbf{g}_i^v\|}$. For details, please refer to [46] and the supplementary material.

Curvature integration Depth images can provide more geometric information other than normals [13, 25]. To solve the biased sampling problem mentioned in Sec. 2.2, we propose directly incorporating mean curvature during the voxelization step to help with the sampling procedure during training. The mean curvature and other differential geometry features, such as the Gaussian curvature, are closely related to principal curvatures, often denoted as κ_1

and κ_2 . The mean curvature H is the average of the principal curvatures, while the Gaussian curvature K is their product. They are both local geometry properties of the surface and reveal the local topology characteristics. In this way, we do not need a ground-truth mesh for computing curvature information. To our knowledge, we are the first to integrate mean curvatures, computed from depth images, with voxels for efficient sampling afterward. A depth image can be viewed as a Monge patch of a surface, i.e. $z = D(m, n)$, $(m, n) \in \Omega \subset \mathbb{R}^2$ with pixel coordinates (m, n) lay in the image domain Ω [14, 47]. Thus, the Monge patch $\mathcal{M} : \Omega \rightarrow \mathbb{R}^3$ is $\mathcal{M}(m, n) = (m, n, D(m, n))$. To compute the two types of curvatures from the depth

$$K(m, n) = \frac{D_{mm}D_{nn} - D_{mn}^2}{(1 + D_m^2 + D_n^2)^2}, \quad (2)$$

$$H(m, n) = \frac{(1 + D_m^2)D_{nn} - 2D_mD_nD_{mn} + (1 + D_n^2)D_{mm}}{2(1 + D_m^2 + D_n^2)^{3/2}}, \quad (3)$$

where $D_m = \frac{\partial D(m, n)}{\partial m}$ is the partial derivative of depth w.r.t. x -axis in the image plane; similarly, $D_n = \frac{\partial D(m, n)}{\partial n}$, $D_{mn} = \frac{\partial^2 D(m, n)}{\partial m \partial n}$ for D_{mm} and D_{nn} . The computation is done on-the-fly per depth image. After associating a curvature to each point from every depth image, we update voxel curvature attributes by averaging all points inside the same voxel $H_i^v = \frac{1}{N} \sum_j H(\mathcal{M}(m, n)_j)$, where i is the voxel index and j is the pixel index. Curvatures are computed using local image coordinates, and we can still fuse curvatures into voxel (world) coordinates because the mean curvature $H(m, n)$ and Gaussian curvature $K(m, n)$ are invariant to changes of the parameterization on the smooth surface represented by $\mathcal{M}(m, n)$ [14]. A detailed explanation is provided in the supplementary material.

Thus, for each voxel, we use a weighted averaging (see the supplementary material) to iteratively update its gradient \mathbf{g}^v , curvature H^v , SDF ψ^v and uncertainty w^v information. The weighted averaging helps to reduce the error caused by computing on the depth images, as depth images could be noisy and sparse. The normal and curvature computation time for a 480×640 depth image, plus updating voxel attributes according to this incoming depth, is **around 50 millisecond**. Fig. 2 displays that the computed curvature indeed captures the local geometric properties of the surface.

3.2. Voxel-based Sampling

Interpolating Sampling

In this section, we introduce an interpolation strategy that deals with the sparse input and uses the gradient and curvature information. With the

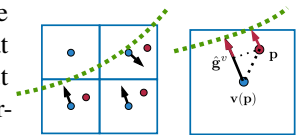


Figure 3. Illustration of (4)

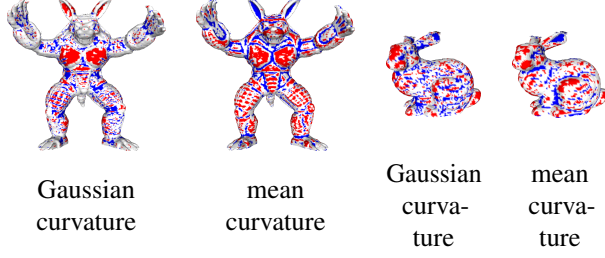


Figure 2. The visualization of Gaussian curvatures and mean curvatures of each point. The red color indicates a high curvature area, and the blue color indicates a low curvature area. A positive mean curvature ($H > 0$) signifies a convex surface, while a negative mean curvature ($H < 0$) indicates a concave surface. Positive Gaussian curvature ($K > 0$) indicates that the surface is locally shaped like a dome or sphere at that point, and negative Gaussian curvature ($K < 0$) indicates that the surface is locally saddle-shaped or hyperbolic at the point.

initialized coarse voxel representation $\{\mathbf{v}_i\}$, we first sample a random point $\mathbf{p} \in \Gamma$ in 3D space, where $\Gamma \subset \mathbb{R}^3$ is the sampling domain. With the help of the voxel grid structure, we can localize in which voxel the point $\mathbf{p} \in \mathbb{R}^3$ lies and denote the coordinate of the voxel center as $\mathbf{v}(\mathbf{p}) \in \mathbb{R}^3$. Then, the signed distance value of the sampled point \mathbf{p} can be easily computed by Taylor expansion with the help of the stored gradient \mathbf{g}^v as Fig. 3

$$\psi^p = \psi^v + \langle \hat{\mathbf{g}}^v, \mathbf{p} - \mathbf{v}(\mathbf{p}) \rangle, \quad (4)$$

where $\hat{\mathbf{g}}^v = \frac{\mathbf{g}^v}{\|\mathbf{g}^v\|}$ is the normalized gradient of the distance field. The uncertainty of the sampled point is interpolated using

$$w^p = \frac{v_s - \psi^p}{v_s} w^v, \quad (5)$$

where v_s is the voxel size, w^v is initial voxel uncertainty as mentioned in Sec. 3.1. The (5) sets the maximum value to the points on the surface ($\psi^p = 0$) and reduces the value when points are moved away from the surface, this is due to the fact that Taylor expansion approximation accuracy reduces along the distance to the interpolated point (note the 0 uncertainty means not reliable). Meanwhile, the point \mathbf{p} inherits the curvatures of its voxel K^v and H^v . Thus, we are not restricted to sampling only from a fixed set of points but can pick any point in the space for training. Furthermore, locating $\mathbf{v}(\mathbf{p})$ can be done by one-step calculation, please see the supplementary material. Our method does not require any additional nearest neighbor search or access to neighbor voxels. The (4) is within its own voxel. Hence it is free from the voxel resolution since the training inputs are point-signed distance value pairs.

Curvature-guided sampling To avoid the uneven sampling problem, we divide sampled points into low, median, and high curvature regions, similar to [35], we use the mean (or Gaussian) curvature instead of principle curvatures. Due

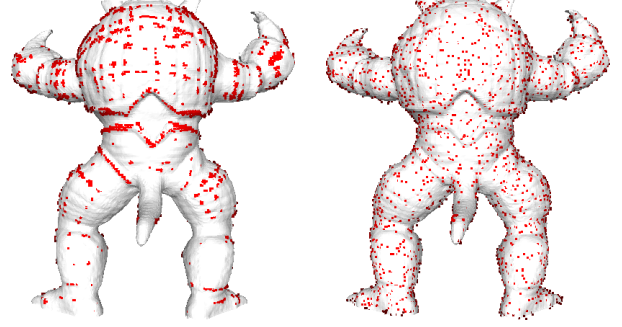


Figure 4. Points gathering on high curvature effect (left) and our sampling results after considering points mean curvature (right).

to the page constraint and the similarity of the mean and Gaussian curvatures (see Fig. 2), in the following, we only show the results based on the mean curvature. For each epoch, m points (see Sec. 3.2) are sampled from low curvature category $\hat{\mathbf{p}} \sim \{\mathbf{p} \in \Gamma \mid H^p < \underline{H}\}$, median curvature category $\hat{\mathbf{p}} \sim \{\mathbf{p} \in \Gamma \mid \underline{H} \leq H^p < \bar{H}\}$, and high curvature category $\hat{\mathbf{p}} \sim \{\mathbf{p} \in \Gamma \mid H^p \geq \bar{H}\}$. The threshold \underline{H} and \bar{H} are chosen by the curvature range of 0.3 and 0.7 percentile. The visualized sampling results are shown in Fig. 4.

3.3. Uncertainty-Aware Implicits

Loss with uncertainty We would like to recover the neural implicit function $f : \mathbb{R}^3 \rightarrow (\psi, w) \subset \mathbb{R} \times [0, 1]$, such that the surface lies on the level-set $\{\mathbf{x} \mid f(\mathbf{x}) \in 0 \times (\tau, 1]\}$, and w is the uncertainty of the predicted signed distance value ψ . τ is the uncertainty threshold. Given a point \mathbf{p} in the sample domain Γ , as described in Sec. 3.2, its corresponding voxel $\mathbf{v}(\mathbf{p})$ with the interpolated SDF value ψ^p and uncertainty w^p (using (4) and (5)), we define the loss function of the geometric and the normal constraints as

$$l_{\mathcal{X}}(\theta) = \frac{1}{|\Gamma^+|} \int_{\Gamma^+} (|\psi - \psi^p|) d\Gamma, \quad (6)$$

$$l_{\mathcal{N}}(\theta) = \frac{1}{|\Gamma^+|} \int_{\Gamma^+} (1 - \langle \frac{\nabla_{\psi} f(\mathbf{p}, \theta)}{\|\nabla_{\psi} f(\mathbf{p}, \theta)\|}, \hat{\mathbf{g}} \rangle) d\Gamma, \quad (7)$$

$$l_{\mathcal{W}}(\theta_r) = \int_{\Gamma} |w - w^p| d\Gamma, \quad (8)$$

$$l_{\mathcal{E}}(\theta) = \int_{\Gamma} \|\nabla_{\psi} f(\mathbf{p}, \theta)\|^2 - 1 d\Gamma, \quad (9)$$

where Γ^+ indicates the area with the sampled uncertainty $w^p > 0$. The (7) evaluates the cosine similarity of surface normal and implicit function gradient. The Eikonal loss term $l_{\mathcal{E}}(\theta)$ guarantees that the optimized neural network represents a signed distance field. The final loss is

$$l(\theta, \theta_r) = l_{\mathcal{X}}(\theta) + \tau_n l_{\mathcal{N}}(\theta) + \tau_w l_{\mathcal{W}}(\theta_r) + \tau_e l_{\mathcal{E}}(\theta). \quad (10)$$

Surface extraction with uncertainty It is reasonable to consider uncertainty when extracting surface using

the Marching cubes algorithm [28], as the uncertainty indicates the reliability of the signed distance value.

Moreover, we also need to deal with the voxel grid with $w = 0$. As shown in Fig. 5, a single zero uncertainty vertex leads to a line (instead of a triangle), while two of this kind lead to a point [3, 16]. Therefore, we can naturally reconstruct open surfaces, thanks to our uncertainty estimation.

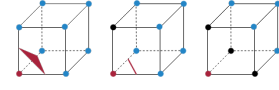


Figure 5. surface extraction with uncertainty. Black vertices represent zero uncertainty points. Red and blue vertex mean points with negative and positive SDF values, respectively.

3.4. Incorporating with Other Methods

Our curvature-guided sampling can seamlessly incorporate popular implicit surface reconstruction methods such as [18, 45]. These methods take point clouds as input. The points with curvature can be extracted using (1) and the geometric loss (6) is

$$l_{\mathcal{X}}(\theta) = \frac{1}{|\mathcal{V}|} \sum_{i \in \mathcal{V}} \|f(\mathbf{x}_i; \theta)\|_1. \quad (11)$$

Additionally, our interpolating method simplifies the method that needs nearest neighbor search, such as Neural-Pull [29]. Neural-Pull proposes to train a network to learn the pulling direction and the distance to the iso-surface. During training, the method samples random points \mathbf{p} and uses nearest neighbor search to find the closest surface point \mathbf{x} . Then, a network f is trained to minimize the loss

$$l_{\mathcal{X}}(\theta) = \frac{1}{|\Gamma|} \int_{\Gamma} \left\| \mathbf{x} - \frac{\nabla f(\mathbf{p})}{\|\nabla f(\mathbf{p})\|} f(\mathbf{p}) \right\| d\Gamma, \quad (12)$$

with $\tau_n = 0$, $\tau_e = 0$. Our interpolating method (Sec. 3.2) eliminates the nearest neighbor search required in the original Neural-Pull. As for a random point \mathbf{p} , after finding the corresponding voxel $\mathbf{v}(\mathbf{p})$, the closest surface point \mathbf{x} can be easily located using (1). In Sec. 4, we show that it effectively reduces the noise during training and leads to better reconstruction quality. The modified Neural-Pull outperformed the original implementation, especially under sparse inputs.

Even though it is based on voxel representation, the proposed sampling method can access surface points without a surface extraction step such as Marching cubes. During the interpolating step, there is no nearest neighbor search or cubic interpolation, which needs to access 8 voxel vertices like in most voxel-based methods. The only interpolation step is done within its voxel by (4). We use this hybrid representation to lead an efficient sampling step.

4. Evaluation

To demonstrate that our sampling method improves the robustness and accuracy of the implicit surface learning. We validate our method on synthetic and real-world datasets, including objects and scene scenarios. For synthetic datasets with ground-truth mesh, we rendered perfect depth images and camera poses using the ground-truth mesh to initialize voxel grid $\{\mathbf{v}_i\}$. To test low-quality input, we initialed two different voxel resolutions, 64^3 (**sparse**) and 256^3 (**dense**), to vary the sparsity of the input. The real-world datasets contain RGB-D sequences with noisy, sparse depth images and noise camera poses. To compare with the method that takes a point cloud as input, the point cloud is extracted from voxels using (1) with normals. We use an 8-layer multi-layer perceptron (MLP) with ReLU activations. Each layer has 256 nodes, and the last layer has 2 output nodes for the SDF and uncertainty. We set the learning rate to 10^{-4} with decay and use the mean curvature for curvature-guided sampling. The batch size is $10k$, and we train for $10k$ epochs for each dataset. Our PyTorch implementation takes approximately 15 minutes to train on a GeForce GTX TITAN X GPU with CUDA for each dataset. All meshes are extracted with the Marching cube algorithm with grid resolution 128^3 . Please note that considering the original input is depth images, with or without camera poses, the initial point cloud is the direct re-projected point cloud using depth images. However, this would cause a noise point cloud without normal information, especially for the real-world dataset. The methods we compared do not emphasize denoising while training. Thus, we use the cleaner point cloud extract from the initialized voxel with normal information for a fair comparison.

4.1. Voxel-based Interpolating Sampling

To verify that interpolating sampling helps when the input data is noisy and sparse, we compare against the classical methods, SSD [4] and Poisson surface reconstruction [24], as well as learning-based methods, IGR [18] and SIREN [45], which take a point cloud **with normals** as the input (We provide the no normal ablation study in the supplementary material). IF-NET [7] also uses a voxelized point cloud as input. We test our method on 4 synthetic datasets to get the quantitative error. After extracting the mesh, we computed the Chamfer distance (CD) and Hausdorff distance (HD) of the reconstructed mesh with respect to the ground-truth mesh in two different input (sparse and dense) resolutions. Fig. 6 shows the visual comparison and the Tab. 1 shows the quantitative comparison. All methods produce satisfactory results when the input points are dense. However, our method still gives satisfactory results when the input is sparse. NDF [8] trains a network to learn UDF of a surface to represent an open surface. However, the output is only a denser point cloud, and we failed to recover the mesh using Ball-Pivoting Algorithm as the author described in the paper.

Metric	Dataset		Method							
			SSD	Poisson	IF-NET	SIREN	IGR	IGR (curv)	OURS	OURS (curv)
CD ($\times 10^2$)	Bunny	sparse	0.204	0.278	0.303	8.745	0.481	0.447	0.068	0.067
		dense	0.224	0.242	0.315	7.582	0.501	0.491	0.073	0.068
	Armadillo	sparse	0.038	0.031	0.025	2.396	0.060	0.034	0.039	0.037
		dense	0.024	0.025	0.026	2.331	0.035	0.034	0.031	0.030
	Dragon	sparse	0.210	0.206	0.158	2.710	0.209	0.198	0.179	0.157
		dense	0.151	0.150	0.181	2.784	0.162	0.154	0.130	0.126
	Happy Buddha	sparse	0.180	0.240	0.258	2.717	0.307	0.259	0.135	0.125
		dense	0.210	0.202	0.258	2.720	0.248	0.240	0.214	0.267
HD	Bunny	sparse	0.057	0.074	0.112	0.817	0.149	0.142	0.026	0.016
		dense	0.071	0.065	0.107	0.816	0.153	0.155	0.020	0.012
	Armadillo	sparse	0.014	0.006	0.007	0.357	0.018	0.008	0.015	0.006
		dense	0.005	0.006	0.004	0.301	0.014	0.013	0.007	0.007
	Dragon	sparse	0.043	0.050	0.037	0.340	0.037	0.039	0.030	0.040
		dense	0.040	0.039	0.036	0.317	0.056	0.045	0.030	0.025
	Happy Buddha	sparse	0.048	0.061	0.059	0.338	0.092	0.081	0.023	0.017
		dense	0.075	0.057	0.058	0.332	0.059	0.057	0.054	0.044

Table 1. Error numbers for our method with (last column) and without curvature sampling (last second column) and comparison methods. It shows that our method achieves better accuracy under sparse and dense inputs.

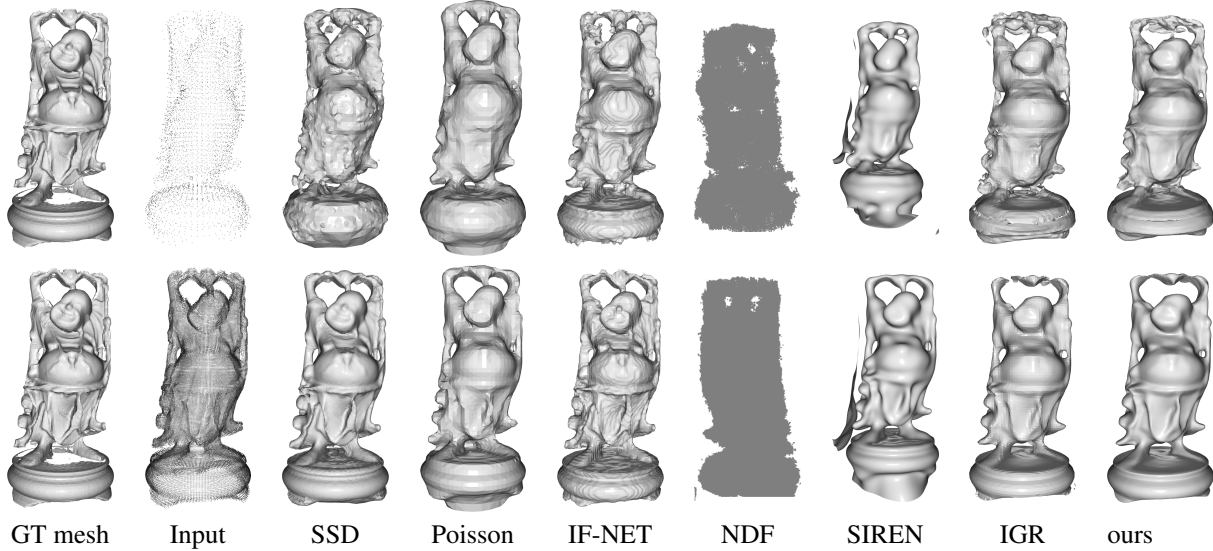


Figure 6. Comparison results with IGR [18], SIREN [45] and IF-NET [7] with two different density input on synthetic datasets. Sparse input *happy_buddha* [12] has $\sim 5k$ points, and dense one has $\sim 96k$ points.

Additionally, we show that our interpolating method improves the previous method. The Neural-Pull method [29] outperforms the methods use (11) as the geometric loss [18, 45], when the normal information is not available. However, nearest neighbor search fails easily when the points are too sparse or noisy, while our interpolating sampling strategy overcomes the problem of sparsity and noise. In Fig. 7, we show the performance of our sampling method with loss (12) compared to the original Neural-Pull method and the baseline method IGR. Our method and Neural-Pull do not use normals in their loss terms, while IGR still uses point normals. The first two rows are synthetic datasets, and the last two rows are real-world datasets *vase* and *sokrates* [51]. These two datasets are RGB-D sequences filming a real object. Each dataset contains around 40 depth images. The noise originates from both the depth images and camera poses. IGR [18] works well for sparse and dense inputs

on synthetic datasets, whereas Neural-Pull fails in sparse situations. Our method compares favorably across all scenarios. Note that the key improvement lays on bypassing the nearest neighbor search step, thus for the works with similar step [27, 30], can easily employ our strategy.

4.2. Random vs. Curvature-Guided Sampling

We show that curvature-guided sampling helps in two aspects. First, it stabilizes the learning procedure, leading to a faster convergence of the minimum solution. We show this visually by rendering reconstructed meshes during early training epochs to see the learning efficiency of the different sampling methods. We compute these rendered meshes' Chamfer distance (CD) and Hausdorff distance (HD) to show that curvature-guided sampling has a smoother error curve. Fig. 9 shows that the network converges faster with curvature sampling than with a random sample. In Fig. 8, the

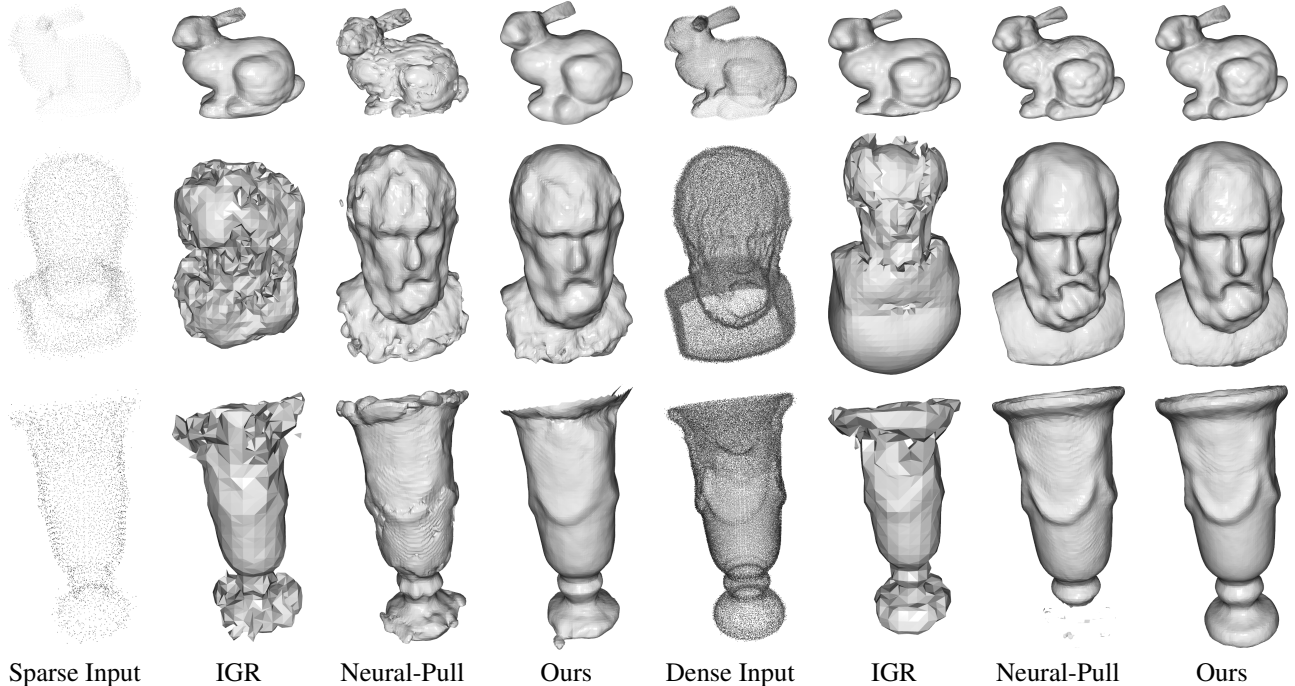


Figure 7. Comparison results with NeuralPull [29] and IGR [18] with two different density input. Sparse input on synthetic dataset *bunny* has $\sim 5k$ points and dense one with $\sim 100k$ points. Two real-world datasets *sokrates* have $\sim 9k$ points and $150k$ points in sparse and dense situations, *vase* has $\sim 4k$ and $\sim 81k$ in two situations. The figure shows the results are largely improved by only changing to our sampling strategies.

solid lines and dash lines are Chamfer distance errors of curvature-guided sampling and random sampling, respectively. We normalized the CD errors by dividing the maximum error within each dataset to draw all lines in one figure. The curvature-guided sampling lines have a smoother trend and reach a lower error faster. Second, we show that curvature-guided sampling also increases the accuracy of reconstructed meshes. We test our method with and without curvature-guided sampling (last two columns in Tab. 1) for a comparison. Moreover, we test on IGR [18] and change its sampling method during training from randomly choosing points to curvature-guided sampling as described in Sec. 3.2 (last third and fourth columns in Tab. 1). Both comparison pairs show that considering curvature information during training improves the results.

4.3. Uncertainty Prediction

In this section, we show the uncertainty prediction result, which illustrates that the uncertainty helps to eliminate redundant areas. We focus on showing the results on the scene dataset to show that with the help of uncertainty, we can also represent an open surface. Many previous works [8, 45] have also trained neural networks to represent scene-level surfaces. However, a method such as [45] produces extra artifacts outside the surface. Although the authors propose one term in the loss function to penalize off-surface points

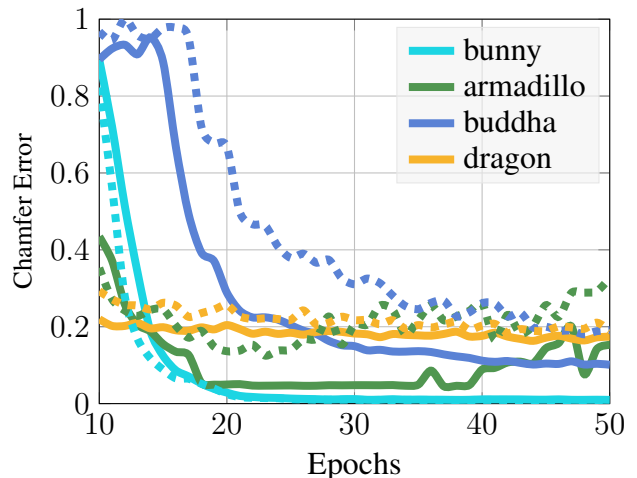


Figure 8. The CD error during different training epochs.

for creating SDF values close to 0, it can not eliminate all artifacts, especially when the input is sparse and noisy. This problem can be solved by considering uncertainty during surface extraction as described in Sec. 3.3. Due to space constraints, we show a subset of comparison results. For more results, please refer to the supplementary material.

5. Conclusion

Summary In this work, we have presented novel curvature-guided sampling methods with uncertainty-augmented surface implicits representation. Our method is easily transfer

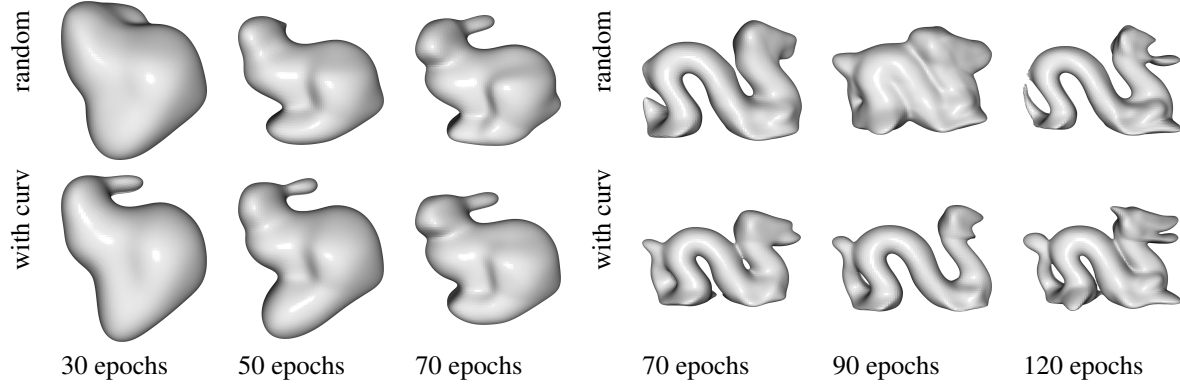


Figure 9. We extract surface during training to compare the effect of curvature-guided sampling and random sampling.

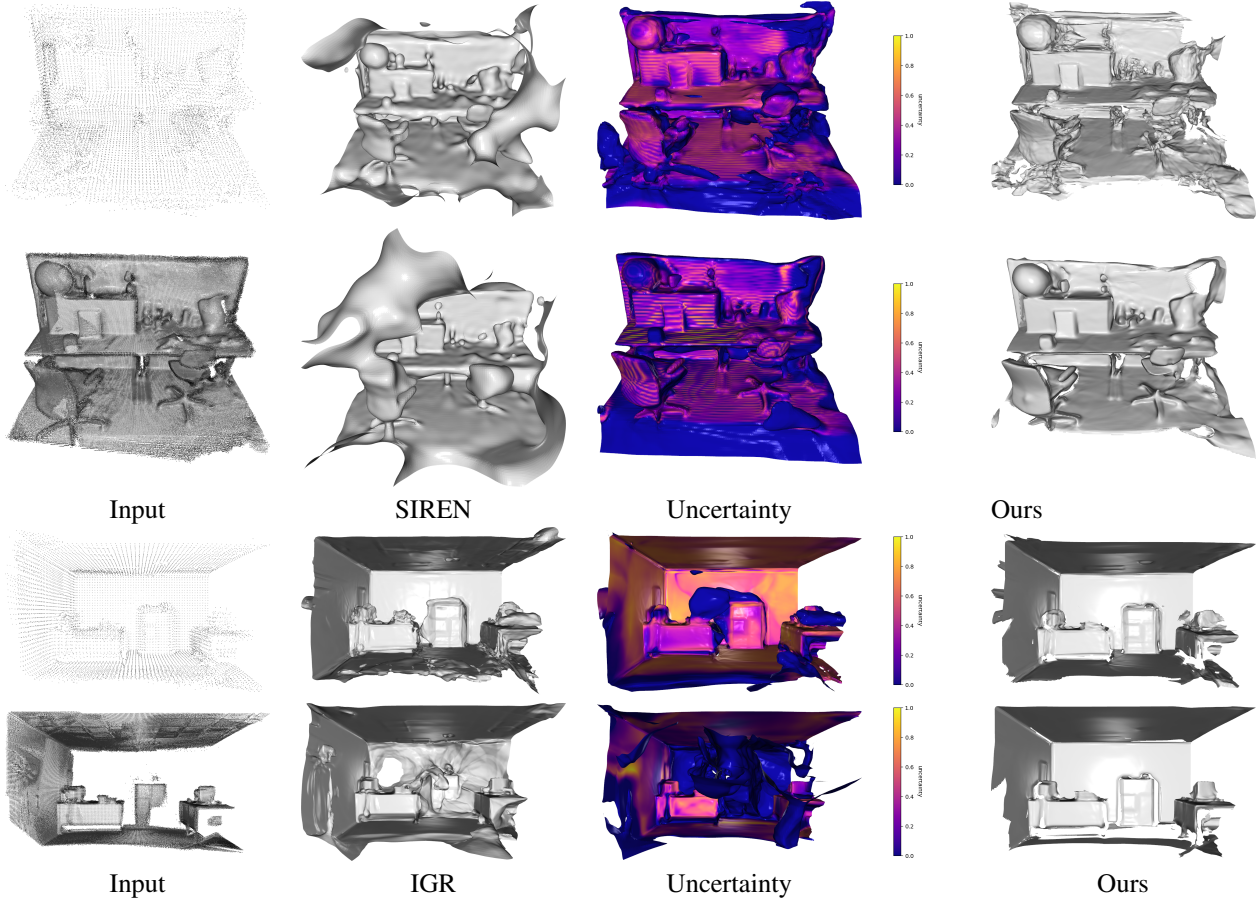


Figure 10. Scene reconstruction results with different density input on real-world dataset *TUM_rgbd* (first two rows, sparse points $\sim 14k$, dense points $\sim 330k$) with noisy camera poses as well. Synthetic dataset *icl_nium* (last two rows, sparse points $\sim 14k$ and dense points $\sim 215k$) with ground truth camera poses.

to exist methods that can efficiently deal with low-quality inputs. Our approach operates on depth images, which can be directly acquired from hardware. We propose a method that computes surface geometric properties: normals and curvatures on depth images instead of using ground truth mesh, which is more suitable for real-world applications. The by-product uncertainty gives a reliability indication for the predicated signed distance value and can help with non-

closed surface representations.

Limitations and future work Our approach does not specialize in surface completion. It will fail to recover any missing areas in depth. Next, since the presented method can be easily integrated with other neural reconstruction methods and shape completion techniques, we plan to incorporate shape completion and neural rendering to deal with missing areas.

A1. Code, Datasets and baseline methods

Our code and evaluation scripts will be publicly available upon acceptance. We will also provide the detailed information about the code of baseline methods.

	name	type	year	link	license
[9]	Redwood	dataset	2016	http://www.redwood-data.org/3dscan/	Public Domain
[12]	The Stanford 3D	dataset	1994	http://graphics.stanford.edu/data/3Dscanrep/	Public Domain
[51]	multi-view dataset	dataset	2015	http://graphics.stanford.edu/projects/vsfs/	CC BY-NC-SA 4.0
[20]	ICL-NUIM	dataset	2014	https://www.doc.ic.ac.uk/~ahanda/VaFRIC/iclnuim.html	CC BY 3.0
[48]	TUM-rgbd	dataset	2012	https://cvg.cit.tum.de/data/datasets/rgbd-dataset	CC BY 4.0
[46]	gradient-SDF	code	2022	https://github.com/c-sommer/gradient-sdf	BSD-3
[18]	IGR	code	2020	https://github.com/amosgropp/IGR	-
[45]	SIREN	code	2019	https://github.com/vsitzmann/siren	MIT license
[7]	IF-NET	code	2020	https://virtualhumans.mpi-inf.mpg.de/ifnets/	-
[29]	Neural-Pull	code	2021	https://github.com/bearprin/neuralpull-pytorch	-
[8]	NDF	code	2020	https://virtualhumans.mpi-inf.mpg.de/ndf/	-
[24]	Poisson	code	2006	http://www.open3d.org/	-
[4]	SSD	code	2011	http://mesh.brown.edu/ssd/software.html	-

Table A.2. Used datasets and code in our submission, together with reference, link, and license. We did our real-world experiments on two datasets, multi-view dataset [51] (for which ground truth poses exist), and Redwood [9] (without ground truth poses). Two synthetic dataset, the Stanford 3D [12], which is an object dataset, and ICL-NUIM dataset [20], which is a scene dataset. For the comparison methods, we use the code listed in the table.

A2. Mathematical detail

A2.1. Math Notations

We summarize important math notation we used in the paper and appendix in Table A.3.

Symbol	Description	Symbol	Description
$\mathbf{x} \in \mathbb{R}^3$	3D points	$\mathcal{P} \subset \mathbb{R}^3$	point cloud set
$\mathcal{V} \subset \mathbb{N}^+$	points index set	$\mathcal{S} \subset \mathbb{R}^3$	continuous surface
$f(\mathbf{x}, \theta)$	neural implicit function	$\theta \in \mathbb{R}^{n \times m}$	learnable parameter
$w^p \in [0, 1]$	points uncertainty	$w^v \in [0, 1]$	voxel uncertainty
$\psi^v \in \mathbb{R}$	voxel SDF value	$\psi^p \in \mathbb{R}$	point SDF value
$\hat{\mathbf{g}}^v \in \mathbb{R}^3$	normalized distance gradient	$\mathbf{g}^v \in \mathbb{R}^3$	voxel distance gradient
∇	differential operator	$H^p \in \mathbb{R}$	point mean curvature
$\Gamma \subset \mathbb{R}^3$	sample domain	$\gamma \in \mathbb{R}$	SDF threshold
$K \in \mathbb{R}$	Gaussian curvature	$H \in \mathbb{R}$	mean curvature
k_1, k_2	principal curvature	$D \subset \mathbb{R}^2$	depth image
$\Omega \subset \mathbb{R}^2$	image domain	$\mathcal{M} \subset \mathbb{R}^3$	Monge path
$d_S(\cdot)$	signed distance to surface \mathcal{S}	$\Gamma^+ \subset \mathbb{R}^3$	sample domain with positive weight
$\bar{H} \in \mathbb{R}$	higher threshold	$\underline{H} \in \mathbb{R}$	lower threshold of curvature
$\mathbf{n}_i \in \mathbb{R}^3$	known points normal	$\mathbf{Q} \in \mathbb{R}^{3 \times 3}$	camera intrinsic matrix
$\mathbf{R} \in SO(3)$	camera rotation matrix	$\mathbf{t} \in \mathbb{R}^3$	camera translation vector

Table A.3. Summary of our notation in the main paper and the supplementary material.

A2.2. Voxelization Details

Given an incoming depth $D(m, n)$, $(m, n) \in \Omega$ with $z = D(m, n) \in \mathbb{R}$ and the estimated pose \mathbf{R}, \mathbf{t} , the 3D points in world coordinates are

$$\mathbf{x} = \mathbf{R}\mathbf{Q}^{-1} \begin{bmatrix} m \\ n \\ 1 \end{bmatrix} z, \quad (13)$$

$$\mathbf{Q} = \begin{bmatrix} f_x & 0 & c_x \\ 0 & f_y & c_y \\ 0 & 0 & 1 \end{bmatrix}, \quad (14)$$

where \mathbf{Q} is the camera intrinsic matrix. Here we describe the standard voxel integration procedure. For each voxel \mathbf{v}_i , we project voxel center to the current depth image using $\mathbf{p} = (p_x, p_y, p_z) = \mathbf{R}^\top(\mathbf{Q}\mathbf{v}_i - \mathbf{t})$ and $(m, n, 1) = \mathbf{p}/p_z$ to find the corresponding pixel coordinates (m, n) on depth, then compare the z -axis value, which stands for the distance of voxel \mathbf{v}_i to the camera center. Then we compute the difference of q_z with depth value on the corresponding pixel, then project is to the normal direction to compute the point-to-plan distance (see (15)). We use convention that inside the surface is positive and outside surface is negative, such that the gradient of SDF have same sign of surface normal. Then, the uncertainty of each voxel is computed using the distance $d_S(\mathbf{v}_i)$. For visible voxel from current depth, which mean $d_S(\mathbf{v}_i)$ is negative, the uncertainty is set to 1, which means this update of distance is valid. To allow some noise, we set the depth integration threshold T (we use $T = 5$) as truncate threshold. If $d_S(\mathbf{v}_i)$ is positive and smaller Tv_s , then the uncertainty drops linearly to 0 (see (17)). Written in more simplified mathematical expression is, the SDF value of points \mathbf{x}_j and its normal \mathbf{n}_j and curvature K_j computed from the depth image D , then the voxel grid $\{\mathbf{v}_i\}$ SDF and uncertainty is computed by

$$d_S(\mathbf{v}_i) = (\mathbf{x}_{j^*} - \mathbf{v}_i)^\top \hat{\mathbf{g}}_i \quad (15)$$

$$\nabla d_S(\mathbf{v}_i) = \mathbf{g}_i = \mathbf{R}\mathbf{n}_{j^*} \quad (16)$$

$$w^v(\mathbf{v}_i) = \begin{cases} 1, & d_S(\mathbf{v}_i) \leq 0 \\ 1 - \frac{d_S(\mathbf{v}_i)}{v_s T}, & 0 < d_S(\mathbf{v}_i) \leq v_s T \\ 0, & \text{else} \end{cases} \quad (17)$$

$$j^* = \arg \min_j \|\mathbf{x}_j - \mathbf{v}_i\| \quad (18)$$

where v_s is the voxel size, $T \in \mathbb{N}^+$ is the truncate voxel number, in this paper, voxel size is set to 0.8cm for 64^3 grid and 0.2cm for 256^3 grid with $T = 5$. Iterating over all depth image, the SDF ψ_i^v , uncertainty w_i^v , gradient \mathbf{g}_i and curvature H_i^v is

updated by

$$\psi_i^v \leftarrow \frac{w_i^v \psi_i^v + w^v(\mathbf{v}_i) d_{\mathcal{S}}(\mathbf{v}_i)}{w_i^v + w^v(\mathbf{v}_i)} \quad (19)$$

$$\mathbf{g}_i \leftarrow \frac{w_i^v \mathbf{g}_i^v + w^v(\mathbf{v}_i) \mathbf{R} \mathbf{g}_i^v}{w_i^v + w^v(\mathbf{v}_i)} \quad (20)$$

$$K_i^v \leftarrow \frac{w_i^v K_i^v + w^v(\mathbf{v}_i) K_{j^*}}{w_i^v + w^v(\mathbf{v}_i)} \quad (21)$$

$$w_i^v \leftarrow w_i^v + w^v(\mathbf{v}_i) \quad (22)$$

The attributes in voxels are integrated using weighted average to be more robust to the noise, especially consider that the normal and curvature are computed using neighborhood information of one pixel on the depth map.

A2.3. Voxel Based Interpolating Sampling Detail

Each property of the voxel grid is stored in a vector. Hence, to get an attribute of one voxel, we need the index of the voxel. Given a random point $\mathbf{p} \in \mathbb{R}^3$, the voxel index (i, j, k) for voxel \mathbf{v} which contain points \mathbf{p} can be localized by

$$(i, j, k) = \text{round}\left(\frac{1}{v_s}(\mathbf{p} - \mathbf{c})\right) \quad (23)$$

where $\mathbf{c} \in \mathbb{R}^3$ is the center coordinates of voxel grid. Thus, we can localize the voxel in one step without any nearest neighbor search.

A2.4. Camera pose estimation

We can estimate camera pose when we initialize the voxel grid using standard Kinect-fusion [34] technique, as described in [46]. We use the first depth map with $\mathbf{R}_0 = \mathbf{I}$ and $\mathbf{t}_0 = \mathbf{0}$ to initial voxel grid as described before in Appendix A2.2, then the initial surface \mathcal{S} is contained in voxels. Then from the second depth, each depth, *e.g.* depth k is an incoming point cloud $\mathcal{P}^k = \{\mathbf{p}_j^k\}_j$ (outside index means iterate over j) after we project them using (13). The problem then is convert to find $\mathbf{R}_k, \mathbf{t}_k$, such that

$$(\mathbf{R}_k, \mathbf{t}_k) = \arg \min_{\substack{\mathbf{R} \in SO(3), \\ \mathbf{t} \in \mathbb{R}^3}} \sum_j w_j d_{\mathcal{S}}(\mathbf{R}_k \mathbf{p}_j^k + \mathbf{t}_k), \quad (24)$$

where $SO(3)$ is 3-dimensional Lie group and $d_{\mathcal{S}}(\mathbf{p})$ denotes the signed distance from the point \mathbf{p} to surface \mathcal{S}

$$|d_{\mathcal{S}}(\mathbf{p})| = \min_{\mathbf{p}_s \in \mathcal{S}} \|\mathbf{p} - \mathbf{p}_s\|. \quad (25)$$

Eq. (24) is solved by Gaussian-Newton and since the gradient $\nabla d_{\mathcal{S}}(\mathbf{p}) = \mathbf{g}$ is pre-computed and stored, it also accelerates the optimization steps, as described in [46]. The camera pose is not given for Redwood [9] (sofa, kiosk, washmachine sequences) and TUM_RGBD [48] (household) datasets, the poses are estimated as described in this section.

A2.5. Proof of the Curvature Integration

In the paper section 3.1, we mention that the transformation between two depth coordinates has non-zero Jacobian (non-zero determinant); hence, integrating curvatures from depth images makes sense. Here is the formulation and proof.

The determinant of the Jacobian of the parameter transformation of the parameterization in the two depth images is non-zero; the mean curvature $H(x, y)$ and Gaussian curvature $K(x, y)$ are invariant.

Proof. Given two depth images D_1 and D_2 taken at two different positions. Suppose the transformation from position 1 to position 2 is a rigid body motion $\mathbf{T} = [\mathbf{R}, \mathbf{t}]$, where $\mathbf{R} \in SO(3)$ is a rotation matrix and $\mathbf{t} \in \mathbb{R}^3$ is a translation vector. Let pixel $p = (m, n)$ in D_1 , $0 \neq z = D_1(m, n)$, and $\mathbf{Q} \in \mathbb{R}^{3 \times 3}$ be the camera intrinsic matrix, then the transformation of pixel p to $\bar{p} = (\bar{x}, \bar{y})$ in D_2 is

$$\begin{bmatrix} \bar{x} \\ \bar{y} \\ 1 \end{bmatrix} = \mathbf{Q} \mathbf{x}, \quad (26)$$

Metric	Dataset	Method (Sparse)					Method (Dense)				
		w/o $l_{\mathcal{E}}$	w/o $l_{\mathcal{W}}$	w/o $l_{\mathcal{N}}$	w/o $l_{\mathcal{N},\mathcal{W}}$	Ours	w/o $l_{\mathcal{E}}$	w/o $l_{\mathcal{W}}$	w/o $l_{\mathcal{N}}$	w/o $l_{\mathcal{N},\mathcal{W}}$	Ours
CD ($\times 10^2$)	Bunny	0.152	0.176	0.171	0.265	0.067	0.153	0.139	0.138	0.395	0.068
	Armadillo	0.089	0.052	0.037	1.180	0.037	0.104	0.041	0.052	1.987	0.030
	Dragon	0.387	0.182	0.226	0.251	0.157	0.138	0.158	0.184	0.196	0.126
	Happy	0.378	0.289	0.467	0.184	0.125	0.248	0.301	0.253	0.295	0.267
	Buddha										
HD	Bunny	0.058	0.044	0.039	0.074	0.016	0.010	0.139	0.012	0.039	0.043
	Armadillo	0.009	0.016	0.006	0.104	0.006	0.019	0.013	0.028	0.251	0.007
	Dragon	0.044	0.038	0.048	0.047	0.030	0.024	0.045	0.065	0.041	0.025
	Happy	0.118	0.057	0.146	0.045	0.017	0.052	0.078	0.053	0.142	0.044
	Buddha										

Table A.4. Ablation study for the individual loss term that we presented on Eq. (10). The error numbers indicate with full losses, the reconstructed meshes are best in most situation quantitatively.

where \mathbf{x} is computed using (13) and \mathbf{Q} is same as (14). is invertible, f_x, f_y is the camera focal length and c_x, c_y is the principal points. The pixel 3D coordinates in under two camera view is $\mathbf{Q}^{-1}(x, y, 1)^{\top} \mathbf{z}$ and $\mathbf{Q}^{-1}(\bar{x}, \bar{y}, 1)^{\top} \bar{\mathbf{z}}$. Let $\{r_{ij}\}_{ij}, i, j \in \{1, 2, 3\}$ be the element in \mathbf{R} and $\mathbf{t} = (t_1, t_2, t_3)^{\top}$, compute the right side, we have $\bar{\mathbf{z}} = r_{31}x + r_{32}y + r_{33}z + t_3$ is the depth value after a rigid body motion and $\bar{\mathbf{z}} \neq 0$ since it does not fall to image plane of D_2 as we assume the point is visible in both camera position.

$$\det(\mathbf{Q}\mathbf{R}\mathbf{Q}^{-1}) = \det(\mathbf{Q})\det(\mathbf{R})\det(\mathbf{Q})^{-1} = 1, \quad (27)$$

it is because $\det(\mathbf{Q}) \neq 0$, $\det(\mathbf{R}) = 1$ and $\det(\mathbf{Q}^{-1}) = \det(\mathbf{Q})^{-1}$. Thus, the transformation Jacobian of the 3D points is non-zero. For the Jacobian of the transformation from (x, y) to (\bar{x}, \bar{y}) , we only need to consider the upper-left 2×2 submatrix of $\mathbf{Q}\mathbf{R}\mathbf{Q}^{-1}$. Since the upper-left 2×2 matrix of \mathbf{R} represents the rotation matrix in the xy plane, thus it is non-zero. The upper-left 2×2 matrix of \mathbf{Q} is diagonal also non-zero. Hence, we get the determinant of Jacobian from (x, y) to (\bar{x}, \bar{y}) is also non-zero. \square

A2.6. Main Curvature Vs. Gaussian Curvature

In this paper, we focus only on main curvature and have not provided ablation study to compare the influence of two curvatures. The reasons are the following. First, from the curvature visualization (Fig. 2 and Fig. A.12), the distribution of low, median and high main curvature and Gaussian curvature are more or less similar. Since we only need the curvature as a guide information to sample points, by control the low, median and high curvature threshold and proportion of each category, using main curvature and Gaussian curvature should not make much difference. Second, from mathematical perspective, main curvature is the addition of two principal curvature, i.e. $H = \frac{k_1+k_2}{2}$ and Gaussian curvature is $K = k_1k_2$. We can have the following bound $-|H| \leq \sqrt{|G|} \leq |H|$. Thus, the difference of using main curvature and Gaussian curvature is negligible.

A3. Loss Function Ablation Study

We have 4 terms in loss function, this part we show how each terms of the loss function influence the results. Tab. A.4 shows the quantitative evaluation on the reconstructed meshes. The Eikonal term (9) ensures that the neural network is indeed a signed distance field. The geometric loss term (6) helps to resolve the orientation ambiguity of the surfaces. The uncertainty term (8) aids get rid of unwanted areas. Additionally, we also examine the interpolation subsampling method under the normal-free situation. Note that even though in our pipeline we have the normal information together with curvature information, since we compute the normal from depth already, we still look into the influence of normal information on sparse and dense input, to show that density of point cloud and normal information are complementary to each other, i.e., dense point cloud helps resolve surface orientation problem. A.5 shows the error table of our method and IGR [18] for with and without geometric loss term. In both table, for some datasets it happens that without geometric loss (6) or without Eikonal loss (9) the error is smaller compared to the full. One possible reason from our analysis is, the function can not satisfy both constrains on some point.

Even one goal of the proposed method is to solve the normal acquisition problem, especially on real world datasets. In the ablation study, we still test the influence of interpolation subsampling on the reconstruction under the normal-free

Metric	Dataset	Method (Sparse)				Method (Dense)			
		w/o l_N		full losses		w/o l_N		full losses	
		IGR [18]	Ours	IGR [18]	Ours	IGR [18]	Ours	IGR [18]	Ours
CD ($\times 10^2$)	Bunny	0.249	0.171	0.481	0.067	0.169	0.139	0.501	0.068
	Armadillo	0.078	0.037	0.060	0.037	0.060	0.052	0.035	0.030
	Dragon	0.225	0.226	0.209	0.157	0.160	0.184	0.162	0.126
	Happy	0.205	0.467	0.307	0.125	0.257	0.253	0.248	0.267
	Buddha								
HD	Bunny	0.109	0.039	0.149	0.016	0.050	0.012	0.153	0.043
	Armadillo	0.032	0.006	0.018	0.006	0.015	0.028	0.014	0.007
	Dragon	0.050	0.048	0.037	0.030	0.046	0.065	0.056	0.025
	Happy	0.074	0.146	0.092	0.017	0.097	0.053	0.059	0.044
	Buddha								

Table A.5. Quantitative comparison with IGR [18] to show the influence of sparse and dense input under no normal information situation.

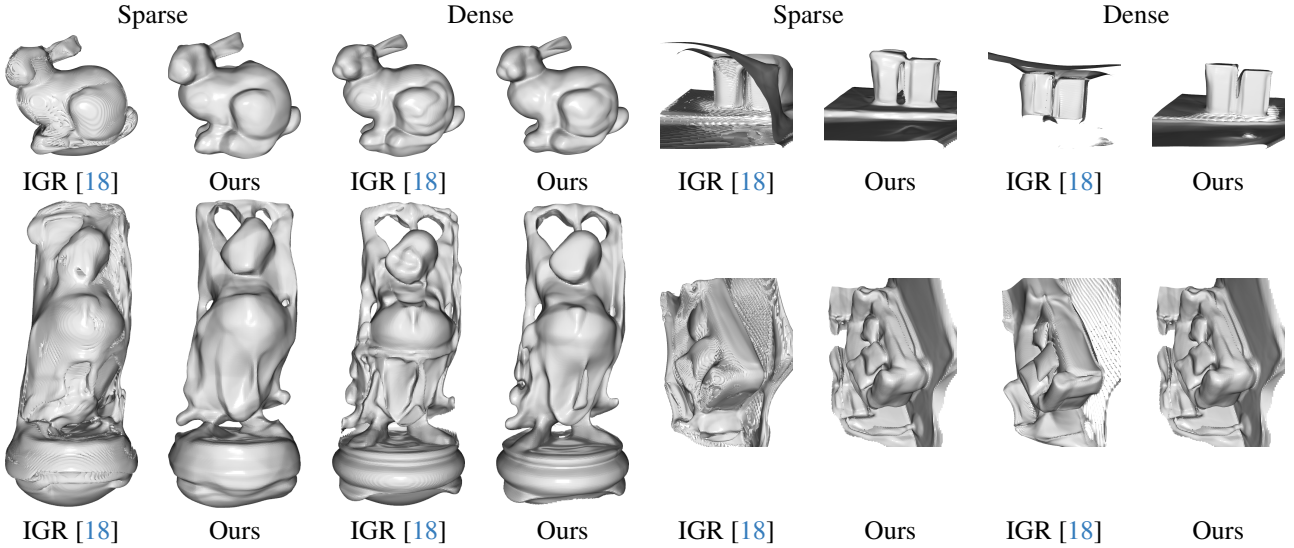


Figure A.11. No normal information reconstruction results on IGR [18] and our method. Our method outperforms IGR on all sparse input situations.

case. Fig. A.11 shows the visualization of two methods, IGR [18] and ours, with $\tau_n = 0$ in (10). It is clear that our method is robust and stable for sparse input even without normal input. IGR can reconstruct satisfactory meshes for dense situation without normal but it fails when the input is sparse, especially when the surface is a planar. Dense input can therefore, resolve ambiguity of the surface orientation to some extent.

A3.1. More Visualization Results

A4. Failing Cases Analysis

[8] shows successful results in ShapeNet [5]. However, we did not get satisfactory results on both object and scene datasets. We suspect the method needs a lot of training data, e.g., ShapeNet has multiple point clouds for a single shape. We only have one (sparse) point cloud for a shape. We also see a similar issue reported in the authors' Github issues. Fig. A.15 shows different failing cases. The first line is the failing case on open surface reconstruction for sparse input ($\sim 6k$) *lr_kit0* datasets. IF-NET [7] can not handle open surfaces. Neural-Pull [29] easily fails when there is a flat plane. SIREN [45] tends to create artifacts in non-surface areas when dealing with open surfaces. The second row is failing cases for complicated shape *Dragon* (sparse input, $\sim 6k$ points). We also fail to recover satisfactory results using our method (last column), and the modified

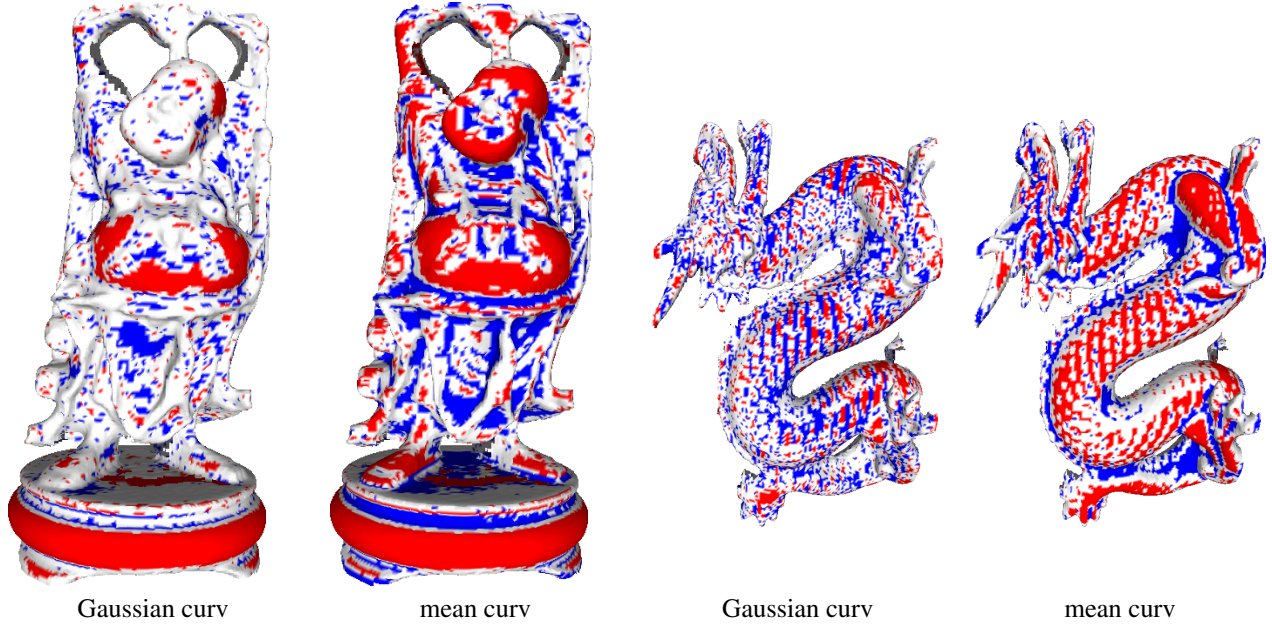


Figure A.12. The visualization of Gaussian curvatures and mean curvatures of *happy_buddha* and *dragon* dataset, computed using depth images as described in main paper section 3.1.

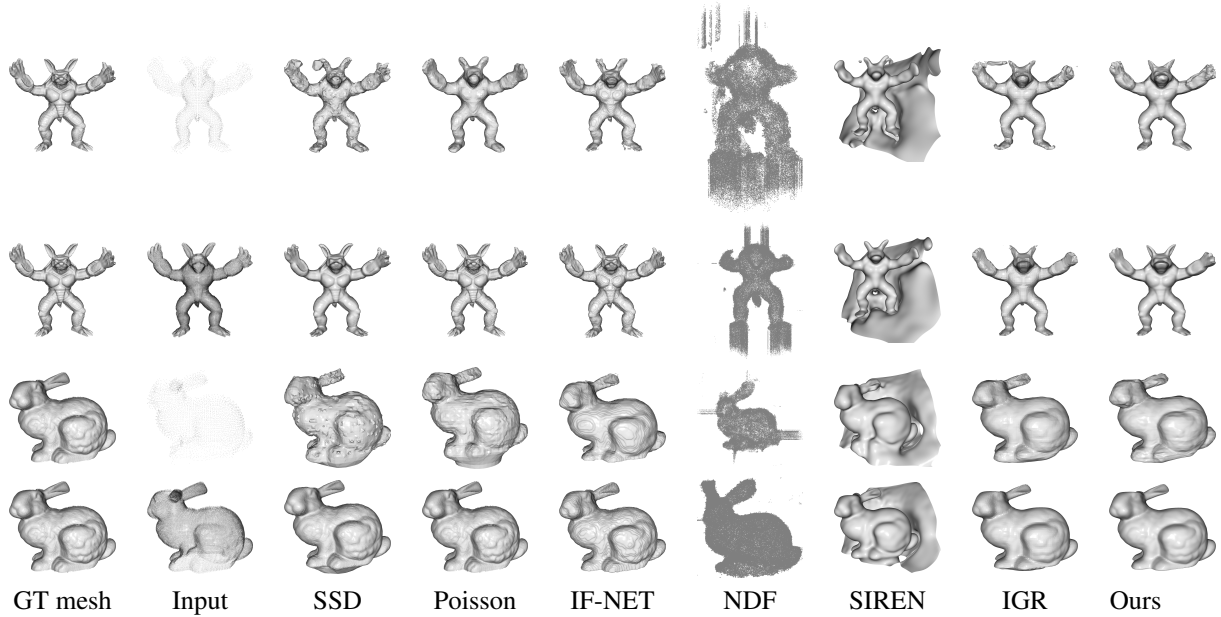


Figure A.13. Comparison results with SSD [4], Poisson surface reconstruction [24], NDF [8], IGR [18], SIREN [45] and IF-NET [7] with two different density input on synthetic datasets [12]. *Armadillo* has $\sim 8k$ in sparse input and $\sim 146k$ in dense input. *Bunny* has $\sim 5k$ sparse points and dense one with $\sim 100k$ points

Neural-Pull method with our sampling strategy also fails to recover the correct shape of the Dragon (last second column). Our analysis is that large details are gathered around the head part of the Dragon, and the interpolation fails to overcome too sparse input.

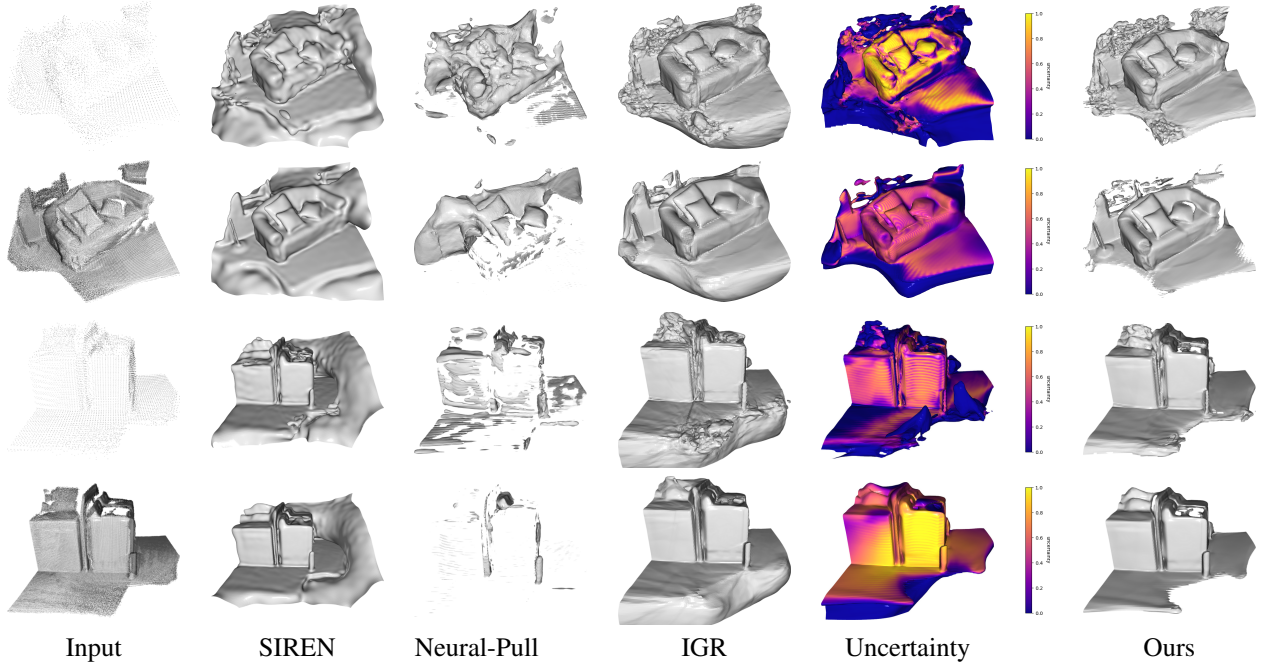


Figure A.14. Two **Real world** Scene datasets [9] results comparison with SIREN [45], Neural-Pull [29] and IGR [18]. Neural-Pull fails in most of the cases, while SIREN creates a redundant area. *Sofa* has $\sim 6k$ points and $\sim 111k$ points in sparse and dense situation, respectively. *Washmachine* with $\sim 8k$ sparse points and $\sim 180k$ dense points.

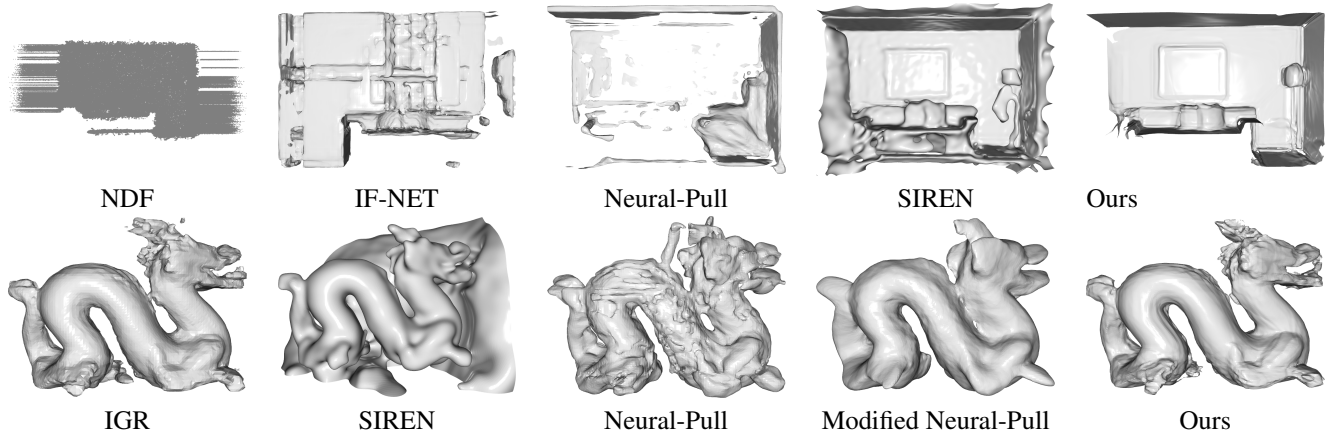


Figure A.15. Failing cases in different methods.

References

- [1] H. Badino, Daniel Huber, Y. Park, and Takeo Kanade. Fast and accurate computation of surface normals from range images. pages 3084 – 3091, 2011. [3](#)
- [2] Fausto Bernardini, Joshua Mittleman, Holly Rushmeier, Claudio Silva, and Gabriel Taubin. The ball-pivoting algorithm for surface reconstruction. *IEEE Transactions on Visualization and Computer Graphics*, 5(4):349–359, 1999.
- [3] M. Botsch, L. Kobbelt, M. Pauly, P. Alliez, and B. Levy. *Polygon Mesh Processing*. CRC Press, 2010. [5](#)
- [4] Fatih Calakli and Gabriel Taubin. Ssd: Smooth signed distance surface reconstruction. *Comput. Graph. Forum*, 30(7):1993–2002, 2011. [2](#), [5](#), [9](#), [14](#)
- [5] Angel X. Chang, Thomas Funkhouser, Leonidas Guibas, Pat Hanrahan, Qixing Huang, Zimo Li, Silvio Savarese, Manolis Savva, Shuran Song, Hao Su, Jianxiong Xiao, Li Yi, and Fisher Yu. Shapenet: An information-rich 3d model repository, 2015. [13](#)

- [6] Zhiqin Chen and Hao Zhang. Learning implicit fields for generative shape modeling. In *2019 IEEE/CVF Conference on Computer Vision and Pattern Recognition (CVPR)*, pages 5932–5941, 2019. [2](#)
- [7] Julian Chibane, Thiemo Alldieck, and Gerard Pons-Moll. Implicit functions in feature space for 3d shape reconstruction and completion. *CoRR*, abs/2003.01456, 2020. [2](#), [5](#), [6](#), [9](#), [13](#), [14](#)
- [8] Julian Chibane, Aymen Mir, and Gerard Pons-Moll. Neural unsigned distance fields for implicit function learning. In *Advances in Neural Information Processing Systems (NeurIPS)*, 2020. [1](#), [2](#), [5](#), [7](#), [9](#), [13](#), [14](#)
- [9] Sungjoon Choi, Qian-Yi Zhou, Stephen Miller, and Vladlen Koltun. A large dataset of object scans. *arXiv:1602.02481*, 2016. [9](#), [11](#), [15](#)
- [10] Solomon Cohen, Leonidas J Guibas, and Olga Sorkine-Hornung. Deep learning with point clouds and earth mover’s distance. 2019.
- [11] Luca Cosmo, Antonio Norelli, Oshri Halimi, Ron Kimmel, and Emanuele Rodolà. LIMP: learning latent shape representations with metric preservation priors. *CoRR*, abs/2003.12283, 2020.
- [12] Brian Curless and Marc Levoy. A volumetric method for building complex models from range images. In *Proceedings of the 23rd Annual Conference on Computer Graphics and Interactive Techniques*, page 303–312, New York, NY, USA, 1996. Association for Computing Machinery. [6](#), [9](#), [14](#)
- [13] J. Matías Di Martino, Alicia Fernández, and José A. Ferrari. 3d curvature analysis with a novel one-shot technique. In *2014 IEEE International Conference on Image Processing (ICIP)*, pages 3818–3822, 2014. [3](#)
- [14] Manfredo P. do Carmo. *Differential geometry of curves and surfaces*. Prentice Hall, 1976. [3](#)
- [15] Marvin Eisenberger, David Novotny, Gael Kerchenbaum, Patrick Labatut, Natalia Neverova, Daniel Cremers, and Andrea Vedaldi. Neuromorph: Unsupervised shape interpolation and correspondence in one go, 2021.
- [16] G.E. Farin. *Curves and Surfaces for CAGD: A Practical Guide*. Elsevier Science, 2002. [5](#)
- [17] Kyle Genova, Forrester Cole, Avneesh Sud, Aaron Sarna, and Thomas A. Funkhouser. Deep structured implicit functions. *ArXiv*, abs/1912.06126, 2019. [2](#)
- [18] Amos Gropp, Lior Yariv, Niv Haim, Matan Atzmon, and Yaron Lipman. Implicit geometric regularization for learning shapes. In *Proceedings of Machine Learning and Systems 2020*, pages 3569–3579. 2020. [1](#), [2](#), [5](#), [6](#), [7](#), [9](#), [12](#), [13](#), [14](#), [15](#)
- [19] A. Handa, T. Whelan, J.B. McDonald, and A.J. Davison. A benchmark for RGB-D visual odometry, 3D reconstruction and SLAM. In *IEEE Intl. Conf. on Robotics and Automation, ICRA*, Hong Kong, China, 2014.
- [20] A. Handa, T. Whelan, J.B. McDonald, and A.J. Davison. A benchmark for RGB-D visual odometry, 3D reconstruction and SLAM. In *IEEE Intl. Conf. on Robotics and Automation, ICRA*, Hong Kong, China, 2014. [9](#)
- [21] Rana Hanocka, Gal Metzger, Raja Giryes, and Daniel Cohen-Or. Point2mesh: a self-prior for deformable meshes. *ACM Transactions on Graphics*, 39(4), 2020. [2](#)
- [22] Fei Hou, Jukai Deng, Xuhui Chen, Wencheng Wang, and Ying He. Neudf: Learning unsigned distance fields from multi-view images for reconstructing non-watertight models, 2023.
- [23] Jiahui Huang, Zan Gojcic, Matan Atzmon, Or Litany, Sanja Fidler, and Francis Williams. Neural kernel surface reconstruction, 2023. [2](#)
- [24] Michael M. Kazhdan, Matthew Bolitho, and Hugues Hoppe. Poisson surface reconstruction. In *Proceedings of the Fourth Eurographics Symposium on Geometry Processing*, pages 61–70, Aire-la-Ville, Switzerland, Switzerland, 2006. Eurographics Association. [2](#), [5](#), [9](#), [14](#)
- [25] Takio Kurita. Computation of surface curvature from range images using geometrically intrinsic weights. 1999. [3](#)
- [26] Loic Landrieu and Mohamed Boussaha. Point cloud oversegmentation with graph-structured deep metric learning. *2019 IEEE/CVF Conference on Computer Vision and Pattern Recognition (CVPR)*, pages 7432–7441, 2019.
- [27] Tianyang Li, Xin Wen, Yu-Shen Liu, Hua Su, and Zhizhong Han. Learning deep implicit functions for 3d shapes with dynamic code clouds, 2022. [6](#)
- [28] William E Lorensen and Harvey E Cline. Marching cubes: A high resolution 3d surface construction algorithm. *ACM siggraph computer graphics*, 21(4):163–169, 1987. [5](#)
- [29] Baorui Ma, Zhizhong Han, Yu-Shen Liu, and Matthias Zwicker. Neural-pull: Learning signed distance functions from point clouds by learning to pull space onto surfaces. *CoRR*, abs/2011.13495, 2020. [5](#), [6](#), [7](#), [9](#), [13](#), [15](#)
- [30] Baorui Ma, Yu-Shen Liu, and Zhizhong Han. Reconstructing surfaces for sparse point clouds with on-surface priors, 2022. [6](#)
- [31] Lars M. Mescheder, Michael Oechsle, Michael Niemeyer, Sebastian Nowozin, and Andreas Geiger. Occupancy networks: Learning 3d reconstruction in function space. *CoRR*, abs/1812.03828, 2018. [2](#)
- [32] Mateusz Michalkiewicz, Jhony K. Pontes, Dominic Jack, Mahsa Baktashmotlagh, and Anders P. Eriksson. Deep level sets: Implicit surface representations for 3d shape inference. *CoRR*, abs/1901.06802, 2019. [2](#)
- [33] Ben Mildenhall, Pratul P. Srinivasan, Matthew Tancik, Jonathan T. Barron, Ravi Ramamoorthi, and Ren Ng. Nerf: Representing scenes as neural radiance fields for view synthesis. In *ECCV*, 2020.
- [34] Richard A Newcombe, Shahram Izadi, Otmar Hilliges, David Molyneaux, David Kim, Andrew J Davison, Pushmeet Kohi, Jamie Shotton, Steve Hodges, and Andrew Fitzgibbon. Kinectfusion: Real-time dense surface mapping and tracking. In *2011 10th IEEE international symposium on mixed and augmented reality*, pages 127–136. Ieee, 2011. [11](#)
- [35] Tiago Novello, Guilherme Schardong, Luiz Schirmer, Vinicius da Silva, Helio Lopes, and Luiz Velho. Exploring differential geometry in neural implicits, 2022. [2](#), [4](#)

- [36] Jeong Joon Park, Peter Florence, Julian Straub, Richard A. Newcombe, and Steven Lovegrove. Deepsdf: Learning continuous signed distance functions for shape representation. *CoRR*, abs/1901.05103, 2019. [2](#)
- [37] Ofir Pele and Michael Werman. A linear time histogram metric for improved sift matching. In *Computer Vision–ECCV 2008*, pages 495–508. Springer, 2008.
- [38] Ofir Pele and Michael Werman. Fast and robust earth mover’s distances. In *2009 IEEE 12th International Conference on Computer Vision*, pages 460–467. IEEE, 2009.
- [39] Songyou Peng, Chiyu "Max" Jiang, Yiyi Liao, Michael Niemeyer, Marc Pollefeys, and Andreas Geiger. Shape as points: A differentiable poisson solver, 2021. [2](#)
- [40] Gabriel Peyré and Marco Cuturi. Computational optimal transport: With applications to data science. *Foundations and Trends® in Machine Learning*, 11(5-6):355–607, 2019.
- [41] Jean Pierre Richa, Jean-Emmanuel Deschaud, François Goulette, and Nicolas Dalmaso. Unsigned distance field as an accurate 3d scene representation for neural scene completion, 2022.
- [42] R. Tyrrell Rockafellar. Hausdorff distance in the space of closed subsets. *Pacific Journal of Mathematics*, 43(2):555–568, 1972.
- [43] Yossi Rubner, Carlo Tomasi, and Leonidas J Guibas. The earth mover’s distance as a metric for image retrieval. *International Journal of Computer Vision*, 40(2):99–121, 2000.
- [44] L Sang, B Haefner, X Zuo, and D Cremers. High-quality rgb-d reconstruction via multi-view uncalibrated photometric stereo and gradient-sdf. In *IEEE Winter Conference on Applications of Computer Vision (WACV)*, Hawaii, USA, 2023.
- [45] Vincent Sitzmann, Julien N.P. Martel, Alexander W. Bergman, David B. Lindell, and Gordon Wetzstein. Implicit neural representations with periodic activation functions. In *Proc. NeurIPS*, 2020. [2](#), [5](#), [6](#), [7](#), [9](#), [13](#), [14](#), [15](#)
- [46] C Sommer, L Sang, D Schubert, and D Cremers. Gradient-SDF: A semi-implicit surface representation for 3d reconstruction. In *IEEE Conference on Computer Vision and Pattern Recognition (CVPR)*, 2022. [3](#), [9](#), [11](#)
- [47] M. Spivak. *A Comprehensive Introduction to Differential Geometry*. Number Bd. 1 in A Comprehensive Introduction to Differential Geometry. Publish or Perish, Incorporated, 1999. [3](#)
- [48] J. Sturm, N. Engelhard, F. Endres, W. Burgard, and D. Cremers. A benchmark for the evaluation of rgb-d slam systems. In *Proc. of the International Conference on Intelligent Robot Systems (IROS)*, 2012. [9](#), [11](#)
- [49] Guandao Yang, Serge Belongie, Bharath Hariharan, and Vladlen Koltun. Geometry processing with neural fields. In *Thirty-Fifth Conference on Neural Information Processing Systems*, 2021. [2](#)
- [50] Lior Yariv, Jiatao Gu, Yoni Kasten, and Yaron Lipman. Volume rendering of neural implicit surfaces. In *Thirty-Fifth Conference on Neural Information Processing Systems*, 2021.
- [51] Michael Zollhöfer, Angela Dai, Matthias Innmann, Chenglei Wu, Marc Stamminger, Christian Theobalt, and Matthias Nießner. Shading-based refinement on volumetric signed distance functions. *ACM Transactions on Graphics (TOG)*, 34(4):1–14, 2015. [6](#), [9](#)